第 44 卷 第 2 期/2024 年 1 月/光学学报 研究论文

光学学报

V_2O_5/SnO_2纳米纤维异质结的构筑及其光电性能

金艳欣，吴邱奇，汤朝阳，曹文君，郭旭达，侯纪伟*

南京工业大学数理科学学院，江苏 南京 211816

摘要 本文使用同轴静电纺丝技术，以合适的钒源和锡源为前驱体，在不同的热处理条件下，制备V_2O_5/SnO_2纳米纤维异质结构，并构筑高灵敏的光电探测器件。在偏置电压为2.0 V、波长为405 nm的激光辐照下，V_2O_5/SnO_2纳米纤维异质结构显示出1.28 μA的光电流，相比纯V_2O_5纳米纤维光电探测器(0.43 μA)，光电流提高了近三倍。在偏置电压为3.0 V的周期性激光的调制下，V_2O_5/SnO_2纳米纤维异质结光电探测器表现出快速的光响应，响应和衰减时间均为0.566 s，响应度为3.97 A/W，比探测率为2.2×10^7 Jones，表现出良好的光电探测性能。这些实验结果为V_2O_5/SnO_2纳米纤维异质结构在光电子器件中的应用提供了新的思路。

关键词 V_2O_5；V_2O_5/SnO_2纳米纤维异质结；静电纺丝；光电探测器

中图分类号 O472+.8 **文献标志码** A **DOI**：10.3788/AOS231260

1 引 言

光电探测器能够将光信号转换成相应的电信号，在环境监测、红外成像、医学诊断和安全通信等领域发挥着关键的作用。随着社会迅速发展，人们对便携、轻量、大面积兼容的可穿戴电子设备的需求不断增加，推动了光电探测器件朝着低成本、高性能、低功耗、大规模制造的方向发展。按照工作机理不同，光电探测器通常可分为热探测器和光子型探测器，其中光子型光电探测器的性能主要取决于半导体活性材料的物理和化学性能。一维无机纳米材料由于大的比表面积、高的长径比、大量的表面陷阱态、独特的电子限域效应有助于电子和空穴的分离，可以有效延长光生载流子的寿命[1-2]。此外，线性的几何结构使其对外部应力具有良好的弹性，在发生形变后不易产生裂纹。这些特性使得一维无机纳米材料成为高性能光电探测器件设计与制备的理想选择[3]。

在一维纳米材料体系中，纳米纤维/线因其独特的电学和光学性质在柔性显示器件、气体传感器件和光电探测器件等领域引起了研究者的浓厚兴趣[4-5]。一维无机纳米材料对不同波长光辐照的响应主要取决于其光学带隙，如宽带隙的ZnO、中等带隙的CdS和窄带隙的VO_2分别对紫外光、可见光和红外光具有很好的响应特性[6-8]。V_2O_5作为过渡族金属氧化物，具有中等直接带隙(2.2～2.8 eV)，在可见光区域具有较大的光学吸收特性，同时具备良好的物理化学性能，被视为优异的光电子器件的候选材料之一[9]。如通过喷雾热解获得的V_2O_5纳米棒对波长为540 nm的可见光表现出良好的响应，高定向的V_2O_5纳米棒薄膜在波长为450 nm的光辐照下表现出优异的光电子特性，V_2O_5纳米线和MoS_2薄膜的复合结构表现出宽光谱的响应性能[10-12]。然而，由于钒具有多种价态，制备V_2O_5纳米纤维存在一定的挑战，这在一定程度上限制了V_2O_5纳米纤维的广泛应用。此外，SnO_2是常见的n型半导体材料，具有很高的电子迁移率(240 $cm^2\cdot V^{-1}\cdot s^{-1}$)，是一种很好的电子传输材料，其空穴电子复合率较低，能够产生稳定的光电流[13]。纳米纤维体系结晶良好，构筑特定功能的异质结可以显著改善其性能，适合制备高性能的光电子探测器件。因此，基于V_2O_5/SnO_2纳米纤维异质结构的光电探测器在理论上应具有比单组分材料更快的光响应速度。

为了进一步研究V_2O_5/SnO_2纳米纤维异质结构的光电子特性，本文使用同轴静电纺丝技术，以不同的钒源和锡源为前驱体，制备具有良好结晶性的V_2O_5/SnO_2纳米纤维异质结构。在不同气氛下进行热退火处理，构筑具有不同形貌尺寸的V_2O_5/SnO_2纳米纤维异质结。然后基于不同形貌尺寸的V_2O_5/SnO_2纳米纤维异质结构，构筑高速光电探测器件，研究其在不同激光辐照条件下对可见光的响应能力，并给出其快速响应的具体物理机制，以扩展V_2O_5/SnO_2纳米纤维异质

收稿日期：2023-07-12；**修回日期**：2023-09-06；**录用日期**：2023-09-15；**网络首发日期**：2023-09-22

基金项目：国家自然科学基金(52002170)、江苏省自然科学基金(BK20190687)、材料化学工程国家重点实验室开放课题(KL19_03)、江苏省研究生与科技实践创新计划(KYCX23_1429)

通信作者：*jwhou@njtech.edu.cn

结的光电应用领域。

2 实　　验

2.1 前驱体溶液的配置

称取 0.7993 g(0.003 mol)乙酰丙酮氧化钒($C_{10}H_{14}O_5V$),$C_{10}H_{14}O_5V$ 从阿拉丁购买,置于小烧杯中,然后用移液枪量取 10 mL 的 N,N-二甲基甲酰胺(DMF),DMF 从百灵威购买,将其滴入上述小烧杯中,使用铝箔封住烧杯口,将其放置在集热式恒温加热磁力搅拌器中,在 75 ℃的温度下加热 10 min,确保 $C_{10}H_{14}O_5V$ 完全溶解。随后向溶解好的 $C_{10}H_{14}O_5V$ 溶液中加入 1.1500 g 聚丙烯腈(10%PAN),PAN 从麦克林购买,置于集热式恒温加热磁力搅拌器中,在 75 ℃的温度下,搅拌 2.5 h,得到具有一定黏度的 PAN+$C_{10}H_{14}O_5V$ 壳层溶液;再称取 1.0607 g(0.003 mol)五水合四氯化锡($SnCl_4·5H_2O$),$SnCl_4·5H_2O$ 从 3A Chem 购买,将其置于小烧杯中,用移液枪量取 10 mL 的 DMF,将其滴入上述小烧杯中,使用铝箔密封烧杯口,并将其放置在集热式恒温加热磁力搅拌器中,在 55 ℃下加热 10 min,以确保 $SnCl_4·5H_2O$ 完全溶解。向溶解好的 $SnCl_4·5H_2O$ 溶液中加入 1.1730 g 聚丙烯腈(10%PAN),置于集热式恒温加热磁力搅拌器中,在 75 ℃的温度下加热搅拌 2.5 h,得到均一的 PAN+$SnCl_4·5H_2O$ 芯层溶液。

2.2 ($PAN+C_{10}H_{14}O_5V$)/($PAN+SnCl_4·5H_2O$)同轴纳米纤维的制备

本实验采用合肥科晶材料技术有限公司生产的 MSK-NFES-1U 型静电纺丝机,22G+17G 同轴不锈钢静电纺丝针头,纺制($PAN+C_{10}H_{14}O_5V$)/($PAN+SnCl_4·5H_2O$)同轴纳米纤维。将配置好的两份溶液分别注入两个注射器中,其中壳层溶液连接同轴针头的外管,芯层溶液注入同轴针头的内管。调节内层纺丝液流速为 0.5 mL/h,外层纺丝液流速为 0.8 mL/h。在电压为 15.06 kV、滚筒收集转速为 200.00 r/min、同轴纺丝针头横向移动速度为 5 mm/s、同轴针头距离滚筒的距离为 20 cm 时,成功纺制出($PAN+C_{10}H_{14}O_5V$)/($PAN+SnCl_4·5H_2O$)同轴纳米纤维。

2.3 V_2O_5/SnO_2 纳米纤维异质结的制备

将纺丝出的原始复合纤维异质结放置于电热鼓风干燥箱中,在 90 ℃下干燥 8 h。再将干燥后的纤维分成两份,分别放入合肥科晶真空管式炉(OTF-1200)进行热退火处理。其中一份置于空气气氛中退火,另一份置于氩气气氛中退火,两者都在 500 ℃时保温 1 h,得到两份不同气氛热退火处理的 V_2O_5/SnO_2 纳米纤维异质结。

3 分析与讨论

图 1 给出了在氩气和空气条件下,V_2O_5/SnO_2 纳米纤维异质结热处理后的 X 射线衍射(XRD)谱图,谱图中的所有衍射峰都可以和正交晶系的 V_2O_5 及金红石型 SnO_2 的衍射峰位匹配,没有别的杂质峰位出现,说明在两种气氛下热处理都得到了高纯的 V_2O_5/SnO_2 纳米纤维异质结构[14-15]。V_2O_5/SnO_2 纳米纤维异质结构使用同轴静电纺丝针头生长,Sn 源前驱体作为核层结构,V 源前驱体作为壳层结构,经过不同的气氛的热处理之后构筑 V_2O_5/SnO_2 纳米纤维异质结构,SnO_2 分布在核层内,V_2O_5 分布在壳层内,最终导致 X 射线衍射谱图中正交系的 V_2O_5 衍射峰明显较多,金红石型 SnO_2 的衍射峰位较少。

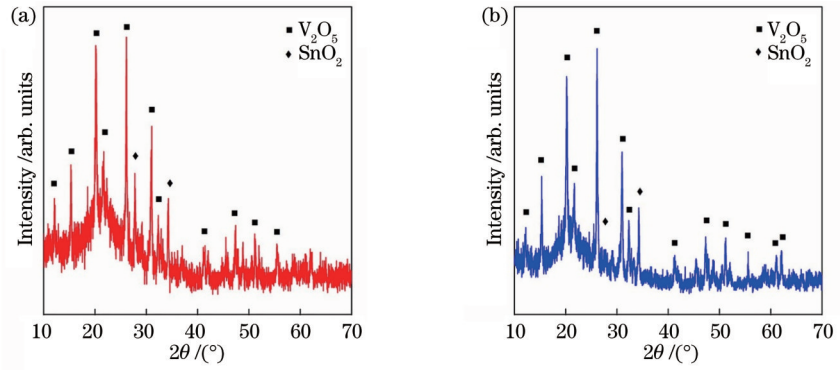

图 1　静电纺丝生长的 V_2O_5/SnO_2 纳米纤维异质结构在不同气氛氛围内热处理的 XRD 图片。(a)空气氛围内热处理;(b)氩气氛围内热处理

Fig. 1　XRD images of electrostatically spun-grown V_2O_5/SnO_2 nanofiber heterostructures heat-treated in different atmospheres. (a) Heat-treated in air atmosphere; (b) heat-treated in argon atmosphere

图 2 给出了在两种气氛下热处理的 V_2O_5/SnO_2 纳米纤维异质结构的场发射电子显微镜(SEM)图片,其中图 2(a)和 2(b)是在氩气中热处理的 V_2O_5/SnO_2 纳米纤维异质结构的不同倍率的 SEM 图片,图 2(c)和 2(d)是在空气中热处理的 V_2O_5/SnO_2 纳米纤维异质结构的不同倍率的 SEM 图片。氩气气氛热处理后,V_2O_5/SnO_2 纳米纤维异质结构保持了良好的线性结构,纤维表面均匀光滑,长度可达数百微米,直径约

1 μm。空气气氛热处理后，V_2O_5/SnO_2纳米纤维异质结构断裂比较明显，静电纺丝生长的长纤维结构几乎均匀断裂，纤维表面出现收缩褶皱，典型的长度为3～5 μm，直径为500 nm左右。纺丝生长的长纤维结构在空气氛围下热处理，部分有机纤维骨架被氧化，导致V_2O_5/SnO_2纳米纤维异质结构断裂和收缩，纤维表面出现收缩褶皱，这一现象在先前的文献中也被报道过[16]。

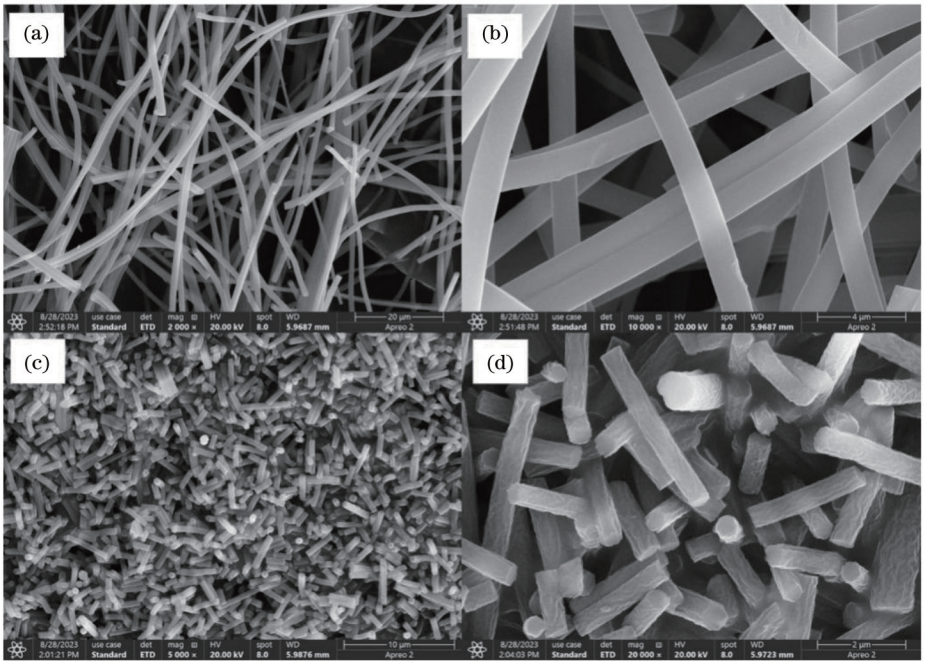

图2 不同气氛氛围热处理下V_2O_5/SnO_2纳米纤维异质结构的SEM图片。(a)低倍率下氩气氛围内热处理SEM图片；(b)高倍率下氩气氛围内热处理SEM图片；(c)低倍率下空气氛围内热处理SEM图片；(d)高倍率下空气氛围内热处理SEM图片

Fig. 2 SEM images of heterogeneous structure of V_2O_5/SnO_2 nanofibers heat-treated in different atmospheres. (a) SEM image of heat-treated in argon atmosphere at low magnification; (b) SEM image of heat-treated in argon atmosphere at high magnification; (c) SEM image of heat-treated in air atmosphere at low magnification; (d) SEM image of heat-treated in air atmosphere at high magnification

为了分析V_2O_5/SnO_2纳米纤维异质结构的元素分布，选取空气氛围下热处理的V_2O_5/SnO_2纳米纤维异质结构进行X射线能量色散光谱(EDS)分析。图3给出了EDS分析的元素分布图。图3(a)是典型的在空气氛围内热处理V_2O_5/SnO_2纳米纤维异质结构的SEM图片，纤维表面存在收缩和褶皱现象。图3(b)是相应的EDS分布，主要的元素为C、O、V、Sn四种，其中Sn元素测试含量相对较少，主要原因是在V_2O_5/SnO_2纳米纤维异质结构中，SnO_2是分布在核层，V_2O_5分布在壳层，这和XRD测试分析的数据一致。图3(c)～(f)分别是V_2O_5/SnO_2纳米纤维异质结构中C、O、V、Sn四种元素的分布图，从图中可以看出，C、O、V、Sn四种元素分布均匀。

图4给出了氩气氛围内热处理得到的V_2O_5/SnO_2纳米纤维异质结构的透射电镜(TEM)图片，图4(a)～(c)分别是不同倍率下的TEM图片。从TEM图片中可以清晰地观察到核壳的双层结构。V_2O_5/SnO_2纳米纤维异质结构使用的是同轴静电纺丝针头生长，Sn源前驱体作为核层结构，V源前驱体作为壳层结构。不同气氛氛围内热处理之后，金红石型的SnO_2主要分布在核层，正交晶系的V_2O_5主要分布在壳层，这和TEM显示的V_2O_5/SnO_2纳米纤维异质结构的核壳结构一致。

为了进一步确定V_2O_5/SnO_2纳米纤维异质结构中的V元素和Sn元素的化学价态，本文对空气氛围内热处理得到的V_2O_5/SnO_2纳米纤维异质结构的样品进行X射线光电子能谱(XPS)分析。图5给出了空气氛围内热处理得到的V_2O_5/SnO_2纳米纤维异质结构的XPS图。图5(a)为XPS全谱图，从XPS全谱图中可以看出，V_2O_5/SnO_2纳米纤维异质结构主要包含C、O、V、Sn、N等元素，其中N元素来源为样品吸附空气中的N_2。如图5(b)所示，$V_{2P1/2}$、$V_{2P3/2}$和O_{1s}的结合能分别523.8、516.2、530.0 eV，其中$V_{2P3/2}$和O_{1s}结合能的差值为13.8 eV，和文献[17]报道的V_2O_5数据一致。图5(c)给出了Sn_{3d}的结合能为495.5 eV，和文献[18]报道的SnO_2数据一致。C的主要来源是纺丝样品中的聚合物碳化，图5(d)给出了C_{1s}的结合能为284.8 eV。XPS元素分析的数据和EDS元素分布的数据一致，进一步证实生长的V_2O_5/SnO_2纳米纤维异质结构是高纯的，不含别的杂质。

为了进一步分析V_2O_5/SnO_2纳米纤维异质结构的光电性能，本文采用氩气氛围内热处理得到的$V_2O_5/$

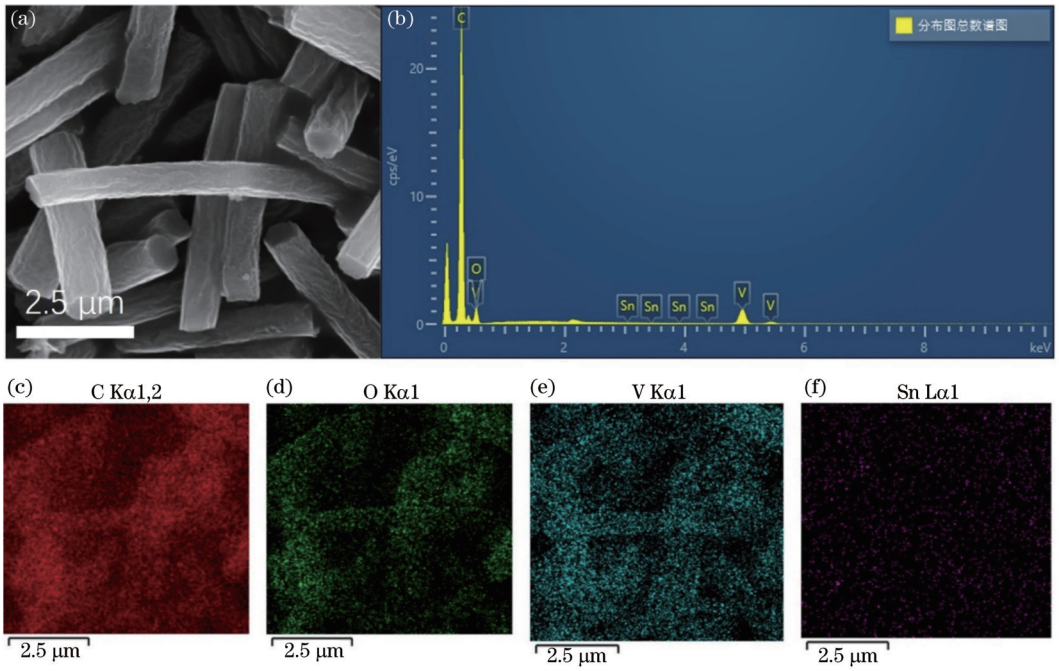

图 3 空气氛围内热处理得到的 V_2O_5/SnO_2 纳米纤维异质结构的 EDS 分析图片。(a)典型的 SEM 图片;(b)EDS 图;(c)C 元素的分布图;(d)O 元素的分布图;(e)V 元素的分布图;(f)Sn 元素的分布图

Fig. 3 EDS analysis images of heterostructure of V_2O_5/SnO_2 nanofibers obtained by heat treatment in air atmosphere. (a) Typical SEM image; (b) EDS image; (c) distribution of element C; (d) distribution of element O; (e) distribution of element V; (f) distribution of element Sn

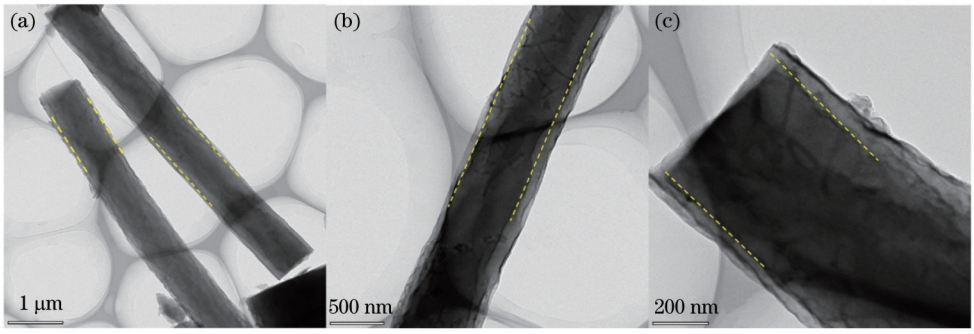

图 4 氩气氛围内热处理得到的 V_2O_5/SnO_2 纳米纤维异质结构的 TEM 图片(其中虚线标出的是核壳结构的分界线)。(a)低倍率下的 TEM 图片;(b)中等倍率下的 TEM 图片;(c)高倍率下的 TEM 图片

Fig. 4 TEM images of heterostructure of V_2O_5/SnO_2 nanofibers obtained by heat treatment in argon atmosphere, where dashed lines mark demarcation line of core-shell structure. (a) TEM image at low magnification; (b) TEM image at intermediate magnification; (c) TEM image at high magnification

SnO_2 纳米纤维异质结来设计两端光电探测器件。首先将 V_2O_5/SnO_2 纳米纤维异质结超声分散在乙醇溶液中,使用胶头滴管滴在清洗干净的硅片表面。使用针尖为 1 μm 的显微钨探针,机械转移 1 根单分散的 V_2O_5/SnO_2 纳米纤维异质结到清洗干净的硅片表面。使用透射电镜铜网微栅作为硬掩模,紧密压实在单根 V_2O_5/SnO_2 纳米纤维异质结表面,然后使用磁控溅射技术溅射 60 nm 的金电极,金电极溅射完成后在体式显微镜下将铜网微栅剥离,使用银胶将铜丝粘贴在金电极表面,即获得 V_2O_5/SnO_2 纳米纤维异质结的两端光电探测器件。其测试原理如图 6(a)所示,实物光学照片如图 6(b)所示。

分别使用型号为 LSR405NL-250-FC 的激光器(λ=405 nm)和 LSR532NL-200-FC 的激光器(λ=532 nm)作为调制光源,研究 V_2O_5/SnO_2 纳米纤维异质结的光电性能,为了作比较,也研究了同样方式生长的纯 V_2O_5 纳米纤维结构。在室温条件下,通过 KEITHLEY-4200 CSC 半导体参数分析仪对所制备的器件进行了 *I-V* 曲线测量。图 7(a)给了两端器件在激光辐照和黑暗下的 *I-V* 曲线,当 V_2O_5/SnO_2 纳米纤维异质结器件存在激光辐照时,器件的光电流明显增强。如施加电压为 2.0 V,在波长为 405 nm、功率为

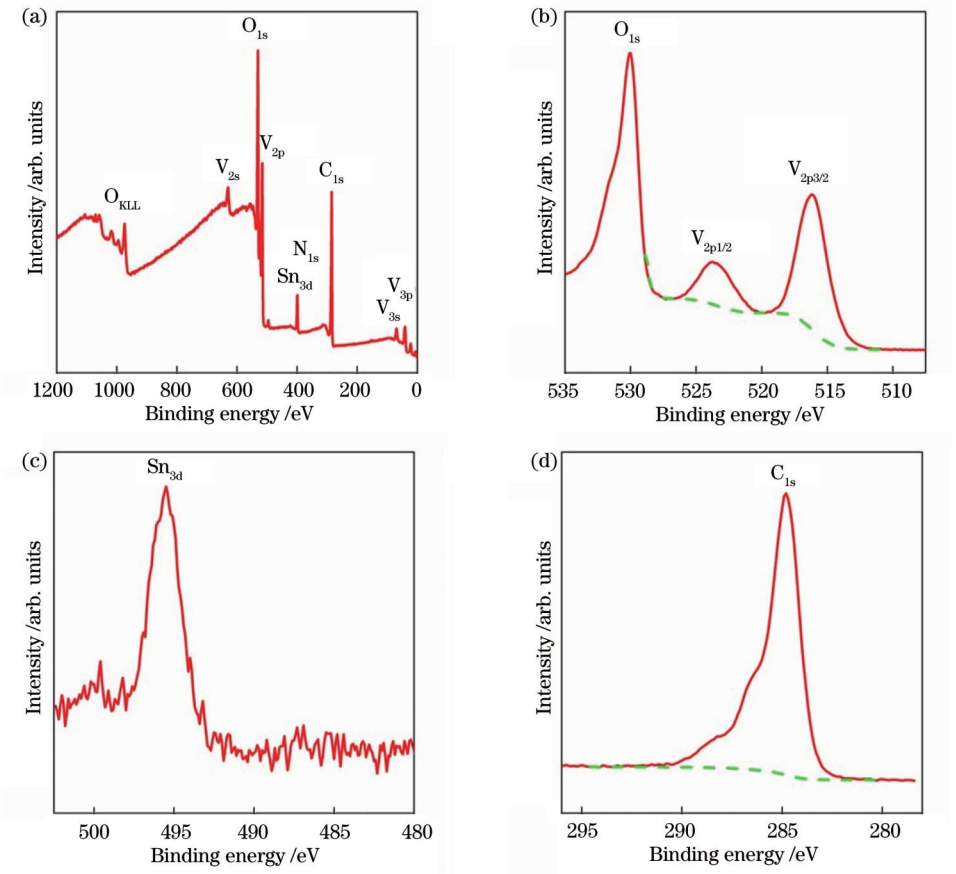

图 5 空气氛围内热处理得到的 V_2O_5/SnO_2 纳米纤维异质结构的 XPS 图。(a)XPS 全谱图;(b)V_{2p} 的结合能;(c)Sn_{3d} 的结合能;(d)C_{1s} 的结合能

Fig. 5 XPS profiles of heterostructures of V_2O_5/SnO_2 nanofibers obtained by heat treatment in air atmosphere. (a) XPS full spectrum; (b) binding energy of V_{2p}; (c) binding energy of Sn_{3d}; (d) binding energy of C_{1s}

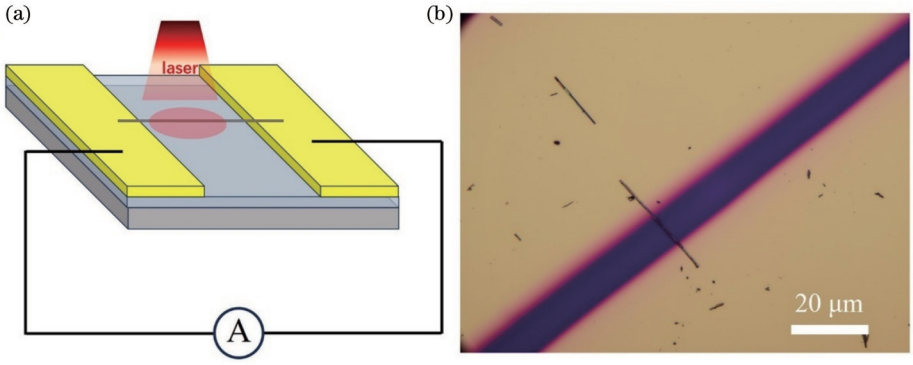

图 6 单根 V_2O_5/SnO_2 纳米纤维异质结光电探测器。(a)光电探测器原理图;(b)光电探测器实物照片

Fig. 6 Single V_2O_5/SnO_2 nanofiber heterojunction photodetector. (a) Schematic diagram of photodetector; (b) physical photo of photodetector

48 mW 的可见光辐照下,异质结显示出 1.28 μA 的光电流,明显高于相同偏置电压下的暗电流(0.96 μA)。作为对比,图 7(b)给出了纯 V_2O_5 纳米纤维器件在相同条件下的光电流和暗电流分别为 0.43 μA 和 0.41 μA,光电流和暗电流差值为 0.02 μA,相比没有明显的变化。

进一步测试分析 V_2O_5/SnO_2 纳米纤维异质结探测器的光响应性能,本文在不同的激光辐照功率下进行了 *I-V* 曲线测试分析。图 8 给出了两种光电探测器件在不同激光辐照功率下的 *I-V* 曲线。从图 8(a)和 8(b)可以明显看出,不同激光辐照功率下光电流与偏压都呈线性关系,说明 V_2O_5/SnO_2 纳米纤维异质结和 V_2O_5 纳米纤维与金电极接触为欧姆接触,不存在明显的势垒,这在很多的文献中都有报道[19-21]。随着激光辐照功率密度的增加,器件光电流迅速增大,这归因于光功率密度增加,V_2O_5/SnO_2 纳米纤维异质结和 V_2O_5 纳米

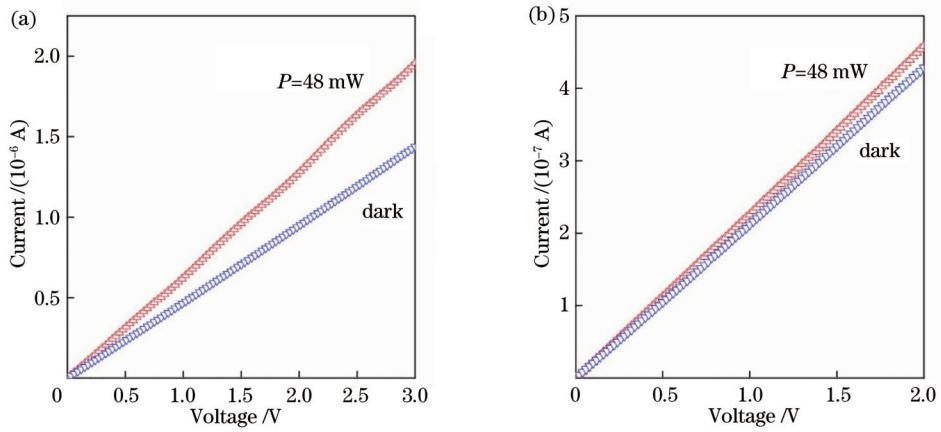

图 7 激光辐照和黑暗条件下两种光电探测器件的 *I-V* 曲线。(a)V_2O_5/SnO_2纳米纤维异质结器件;(b)V_2O_5纳米纤维器件

Fig. 7 *I-V* curves of two photodetectors under laser irradiation and dark conditions. (a) V_2O_5/SnO_2 nanofiber heterojunction device; (b) V_2O_5 nanofiber device

纤维吸收更多的光子,产生更多的空穴和载流子,导致光生载流子密度的增加。对比两种光电探测器件可知,在相同的激光辐照条件下,V_2O_5/SnO_2纳米纤维异质结光电探测器件的光电流明显大于V_2O_5纳米纤维光电探测器,主要原因在于SnO_2是电子传输材料,具有很高的电迁移率,V_2O_5/SnO_2纳米纤维异质结中的光生电子可以被迅速地传输走,从而降低了光生电子和空穴的复合速度,增加了载流子浓度[22-23]。

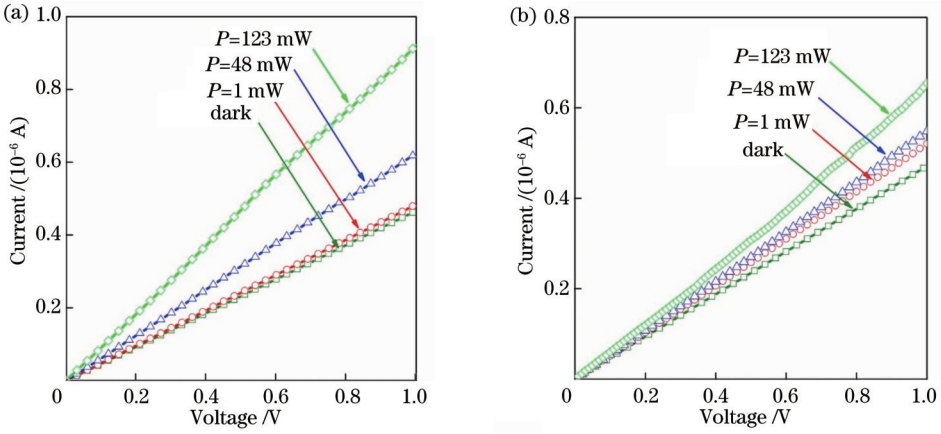

图 8 不同激光辐照功率下两种光电探测器件的 *I-V* 曲线。(a)V_2O_5/SnO_2纳米纤维异质结器件;(b)V_2O_5纳米纤维器件

Fig. 8 *I-V* curves of two photodetectors under different laser irradiation powers. (a) V_2O_5/SnO_2 nanofiber heterojunction device; (b) V_2O_5 nanofiber device

偏置电压为 3.0 V 时,波长为 405 nm、功率为 123 mW 和波长为 532 nm、功率为 92 mW 的两种激光辐照下的动态光电流分别如图 9(a)和 9(b)所示。两束激光分别被周期性开关调制,开关调制的周期为 20 s,随着激光辐照周期性地开和关,器件中的光电流显示出与光照周期性变化相对应的良好可重复性,在观测的周期内,光电流几乎没有任何衰减,显示出良好的稳定性及光电开关性能,与文献报道的钒氧化合物光电探测器一致[24-25]。光开关比(I_{light}/I_{dark})、响应度(R)和比探测率(D^*)是反映光电探测器性能的主要指标:光开关比是光电流与暗电流的比值;响应度是反映将光信号转化为电信号的能力;比探测率则用来反映检测弱信号的能力。其中响应度和比探测率可以通过下式[26-27]计算得到:

$$R=\frac{I_{light}-I_{dark}}{A\times P}, \tag{1}$$

$$D^*=\frac{R}{\sqrt{2e\times I_{dark}/A}}, \tag{2}$$

式中:I_{light}是光电流;I_{dark}是暗电流;P是光功率密度;A是光敏有效区域面积;e是电子电量。从图 10(a)可知,在偏置电压为 3.0 V 时,波长为 405 nm、功率密度为 123 mW 的激光辐照下,V_2O_5/SnO_2纳米纤维异质结光电探测器的光开关比$\frac{I_{light}}{I_{dark}}=1.9$,响应度$R=3.97$ A/W,比探测率$D^*=2.2\times10^7$ Jones。

图 10(a)和 10(b)分别显示在偏置电压为 3.0 V 时,波长为 405 nm、激光功率为 123 mW 的激光辐照下,两种光电探测器单个周期内的动态光电流。光电

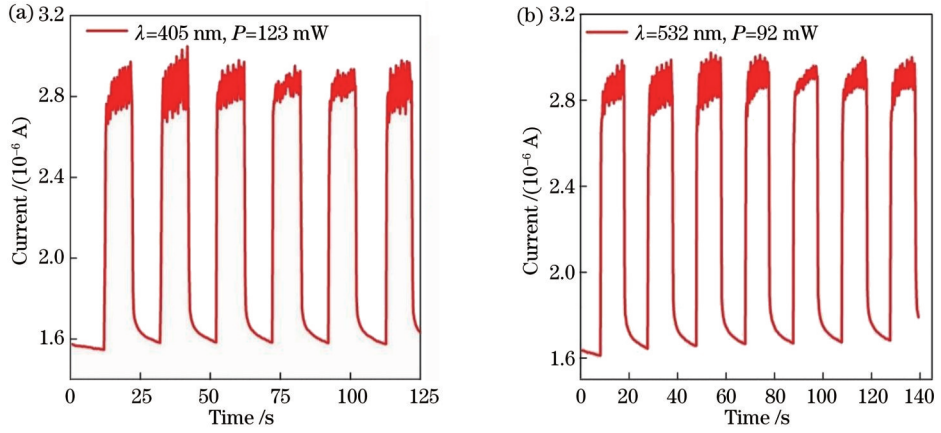

图 9　偏置电压为 3.0V 时，不同激光辐照下光电流随时间的变化关系。(a)波长为 405 nm、功率为 123 mW 的激光辐照；(b)波长为 532 nm、功率为 92 mW 的激光辐照

Fig. 9　Photocurrent versus time for different laser irradiations with a bias voltage of 3.0 V. (a) Laser irradiation with a wavelength of 405 nm and a power of 123 mW; (b) laser irradiation with a wavelength of 532 nm and a power of 92 mW

响应速度是光电探测器的一个重要指标，包括光电响应时间和衰减时间。通常定义光电流增加 10%～90% 所用的时间为光电探测器的响应时间，同理光电流衰减 10%～90% 所用的时间定义为光电探测器的衰减时间。图 10(a)给出了 V_2O_5/SnO_2 纳米纤维异质结光电探测器的响应和衰减时间均为 0.556 s，高于以往文献报道的响应和衰减时间[28]，同时图 10(b)也给出了相同条件下 V_2O_5 纳米纤维光电探测器的响应时间和衰减时间分别为 1.39 s 和 2.78 s。V_2O_5 和 SnO_2 复合之后，光电流响应时间和衰减时间都明显地提升，主要归因于 SnO_2 和 V_2O_5 之间的界面相互作用，光生电子和空穴可以快速地建立平衡。

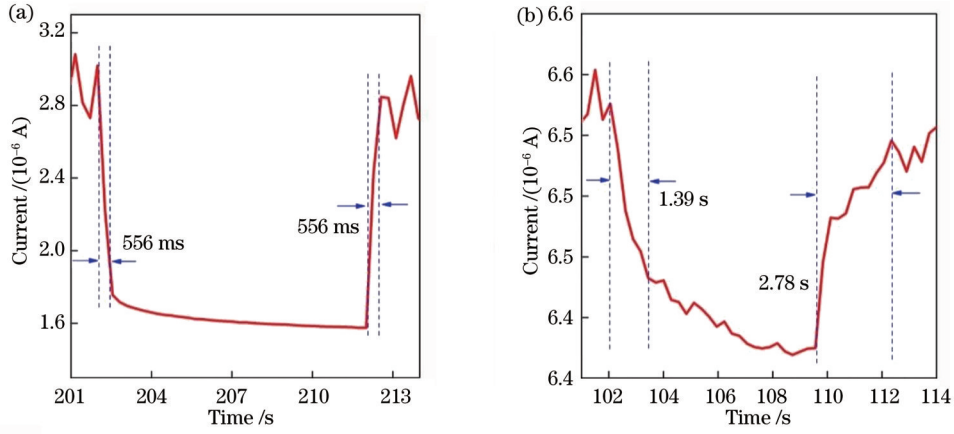

图 10　偏置电压为 3.0 V 时，波长为 405 nm、功率为 123 mW 的激光辐照下，两种光电探测器件的单个循环动态光电流。(a)V_2O_5/SnO_2 纳米纤维异质结器件；(b)V_2O_5 纳米纤维器件

Fig. 10　Individual cyclic dynamic photocurrents of two photodetectors under laser irradiation with a wavelength of 405 nm and a power of 123 mW when bias voltage is 3.0 V. (a) V_2O_5/SnO_2 nanofiber heterojunction device; (b) V_2O_5 nanofiber device

为了深入理解 V_2O_5/SnO_2 异质结快速探测的工作机理，图 11 给出了 V_2O_5/SnO_2 纳米纤维异质结的能带结构示意图。V_2O_5 和 SnO_2 带隙分别为 2.4 eV 和 4.0 eV，因为禁带宽度的不同，当两者接触形成异质界面结构时，会在接触面附近形成Ⅱ型能带弯曲排列并产生内建电场，V_2O_5/SnO_2 材料中的光生电子和空穴在其在Ⅱ型能带排列和内建电场的作用下，纳米纤维异质结中的电子和空穴被分离[29-34]。当纳米纤维异质结受到可见光辐射时，V_2O_5 和 SnO_2 的价带中的电子将发生跃迁至导带中，同时在价带中留下空穴。由于存在能量差异，光生载流子电子会从 V_2O_5 的导带转移到 SnO_2 的导带中，从而被 SnO_2 快速传输走，而空穴则从 SnO_2 的价带转移到 V_2O_5 的价带中。显然，这种Ⅱ型能带对齐的氧化物异质界面有效降低了电子和空穴的复合率，延长了光生载流子的寿命，使得异质结器件的光响应明显优于单一组分器件。

4　结　　论

本文采用同轴静电纺丝技术成功制备了 V_2O_5/SnO_2 纳米纤维异质结构，基于该异质结构设计了光电

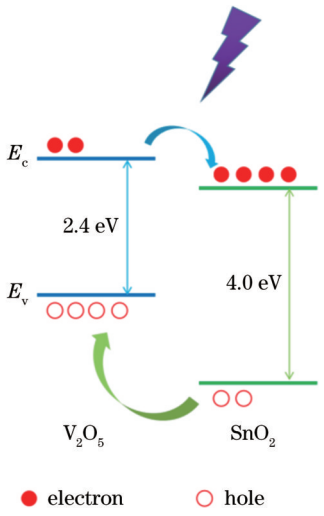

图 11 V_2O_5/SnO_2异质结构形成的Ⅱ型能带排列示意图

Fig. 11 Schematic illustration of type Ⅱ band arrangement formed by V_2O_5/SnO_2 heterojunction

探测器件，并研究了在不同光照条件激励下V_2O_5/SnO_2纳米纤维异质结构光电探测器的光响应性能。实验结果显示，在偏置电压为3.0 V时，周期性激光调制下，V_2O_5/SnO_2纳米纤维异质结光电探测器表现出快速的光响应，响应和衰减时间均为0.566 s，响应度为3.97 A/W，比探测率为2.2×10^7 Jones，在室温条件下表现出良好的光电探测性能。这种高性能归因于在具有Ⅱ型能带对齐的氧化物异质界面处快速且有效的光生激子解离。该研究为氧化物异质结构在光电子器件中的应用提供了新的思路。

参 考 文 献

[1] Zhai T Y, Li L, Ma Y, et al. One-dimensional inorganic nanostructures: synthesis, field-emission and photodetection[J]. Chemical Society Reviews, 2011, 40(5): 2986-3004.

[2] Lou Z, Shen G Z. Flexible photodetectors based on 1D inorganic nanostructures[J]. Advanced Science, 2016, 3(6): 1500287.

[3] 陈荣鹏, 冯仕亮, 郑天旭, 等. Ag纳米线增强硒微米管/聚噻吩自驱动光电探测器性能[J]. 发光学报, 2022, 43(8): 1273-1280.
Chen R P, Feng S L, Zheng T X, et al. Ag nanowires enhance performance of self-powered photodetector based on selenium microtube/polythiophene[J]. Chinese Journal of Luminescence, 2022, 43(8): 1273-1280.

[4] Wang X, Tian W, Liao M Y, et al. Recent advances in solution-processed inorganic nanofilm photodetectors[J]. Chemical Society Reviews, 2014, 43(5): 1400-1422.

[5] Hou J W, Wang B B, Ding Z J, et al. Facile fabrication of infrared photodetector using metastable vanadium dioxide VO_2 (B) nanorod networks[J]. Applied Physics Letters, 2017, 111(7): 072107.

[6] 段雨晗, 蒋大勇, 赵曼. 高增益ZnO肖特基紫外光电探测器光响应特性研究[J/OL]. 发光学报, 2023: 1-9[2023-02-04]. https://cjl.lightpublishing.cn/zh/article/doi/10.37188/CJL.20230169/.
Duan Y H, Jiang D Y, Zhao M. Responsivity characteristics of ZnO Schottky ultraviolet photodetectors with high gain[J/OL]. Chinese of Journal Luminescence, 2023: 1-9[2023-02-04]. https://cjl.lightpublishing.cn/zh/article/doi/10.37188/CJL.20230169/.

[7] Cao F R, Meng L X, Wang M, et al. Gradient energy band driven high-performance self-powered perovskite/CdS photodetector[J]. Advanced Materials, 2019, 31(12): 1806725.

[8] Hou J W, Wang Z P, Ding Z J, et al. Facile synthesize VO_2 (M1) nanorods for a low-cost infrared photodetector application [J]. Solar Energy Materials and Solar Cells, 2018, 176: 142-149.

[9] Yalagala B P, Sahatiya P, Kolli C S R, et al. V_2O_5 nanosheets for flexible memristors and broadband photodetectors[J]. ACS Applied Nano Materials, 2019, 2(2): 937-947.

[10] Abd-Alghafour N M, Ahmed N M, Hassan Z. Fabrication and characterization of V_2O_5 nanorods based metal-semiconductor-metal photodetector[J]. Sensors and Actuators A: Physical, 2016, 250: 250-257.

[11] Wang S T, Wu L F, Zhang H, et al. Facile synthesis of two dimensional (2D) V_2O_5 nanosheets film towards photodetectors [J]. Materials, 2022, 15(23): 8313.

[12] Sahatiya P, Reddy K C S, Badhulika S. Discretely distributed 1D V_2O_5 nanowires over 2D MoS_2 nanoflakes for an enhanced broadband flexible photodetector covering the ultraviolet to near infrared region[J]. Journal of Materials Chemistry C, 2017, 5(48): 12728-12736.

[13] 邵婷婷, 张富春, 崔红卫. Sb掺杂SnO_2的电学性质和光学性质密度泛函理论研究(英文)[J]. 激光与光电子学进展, 2015, 52(8): 081601.
Shao T T, Zhang F C, Cui H. Density functional theory study on the electronic structure and optical properties of Sb-doped SnO_2[J]. Laser & Optoelectronics Progress, 2015, 52(8): 081601.

[14] Yue Y, Liang H. Micro-and nano-structured vanadium pentoxide (V_2O_5) foe electrodes for lithium -ion batteries[J]. Advanced Energy Materials, 2017, 7: 1602545.

[15] Xiong L B, Guo Y X, Wen J, et al. Review on the application of SnO_2 in perovskite solar cells[J]. Advanced Functional Materials, 2018, 28(35): 1802757.

[16] Li Y, Zhu J D, Cheng H, et al. Developments of advanced electrospinning techniques: a critical review[J]. Advanced Materials Technologies, 2021, 6(11): 2100410.

[17] Li X Y, Liu C F, Zhang C K, et al. Effects of preinserted Na ions on Li-ion electrochemical intercalation properties of V_2O_5 [J]. ACS Applied Materials & Interfaces, 2016, 8(37): 24629-24637.

[18] Babu B, Neelakanta R I, Yoo K, et al. Bandgap tuning and XPS study of SnO_2 quantum dots[J]. Materials Letters, 2018, 221: 211-215.

[19] Ma H, Hou J W, Wang X W, et al. Flexible, all-inorganic actuators based on vanadium dioxide and carbon nanotube bimorphs[J]. Nano Letters, 2017, 17(1): 421-428.

[20] Hou J W, Wang X, Fu D Y, et al. Modulating photoluminescence of monolayer molybdenum disulfide by metal-insulator phase transition in active substrates[J]. Small, 2016, 12(29): 3976-3984.

[21] 魏瑶琪, 全家乐, 赵庆强, 等. 一种基于n-ZnS/p-CuSCN纳米薄膜的高开关比和稳定性紫外光电探测器[J]. 发光学报, 2022, 43(6): 911-921.
Wei Y Q, Quan J L, Zhao Q Q, et al. A stable UV photodetector based on n-ZnS/p-CuSCN nanofilm with high on/off ratio[J]. Chinese Journal of Luminescence, 2022, 43(6): 911-921.

[22] Shafique S, Yang S M, Iqbal T, et al. Improving the performance of V_2O_5/rGO hybrid nanocomposites for photodetector applications[J]. Sensors and Actuators A: Physical, 2021, 332: 113073.

[23] Chen H, Hu L F, Fang X S, et al. General fabrication of monolayer SnO_2 nanonets for high-performance ultraviolet

photodetectors[J]. Advanced Functional Materials, 2012, 22(6): 1229-1235.
[24] Chen R S, Wang W C, Chan C H, et al. Photoconductivities in monocrystalline layered V_2O_5 nanowires grown by physical vapor deposition[J]. Nanoscale Research Letters, 2013, 8(1): 443.
[25] Yuan Z Q, Hou J W, Liu K. Interfacing 2D semiconductors with functional oxides: fundamentals, properties, and applications[J]. Crystals, 2017, 7(9): 265.
[26] Hou H Y, Tian S, Ge H R, et al. Recent progress of polarization-sensitive perovskite photodetectors[J]. Advanced Functional Materials, 2022, 32(48): 2209324.
[27] 张翼鹏, 王雪, 纪佩璇, 等. 不同响应机制下的石墨烯基光电探测器研究进展[J]. 发光学报, 2022, 43(4): 552-575.
Zhang Y P, Wang X, Ji P X, et al. Research progress of graphene based photodetectors under different response mechanisms[J]. Chinese Journal of Luminescence, 2022, 43(4): 552-575.
[28] Fu W B, Shang G L, Gong X X, et al. Preparation of large scale and highly ordered vanadium pentoxide (V_2O_5) nanowire arrays towards high performance photodetectors[J]. Journal of Materials Chemistry C, 2017, 5(6): 1471-1478.
[29] 何嘉玉, 陈克强, 冀婷, 等. 基于二维材料的快速响应金属-半导体-金属结构光电探测器研究进展[J]. 发光学报, 2022, 43(5): 745-762.
He J Y, Chen K Q, Ji T, et al. Research progress of fast response 2D material photodetectors with metal-semiconductor-metal structure[J]. Chinese Journal of Luminescence, 2022, 43(5): 745-762.
[30] Chen H Y, Liu K W, Hu L F, et al. New concept ultraviolet photodetectors[J]. Materials Today, 2015, 18(9): 493-502.
[31] 于平平, 段伟, 姜岩峰. 基于Se/TiO_2纳米纤维的自驱动光电探测器特性[J]. 光学学报, 2022, 42(14): 1404001.
Yu P P, Duan W, Jiang Y F. Characteristics of self-driven photodetector based on Se/TiO_2 nanofibers[J]. Acta Optica Sinica, 2022, 42(14): 1404001.
[32] 王江, 罗林保. 基于氧化镓日盲紫外光电探测器的研究进展[J]. 中国激光, 2021, 48(11): 1100001.
Wang J, Luo L B. Advances in Ga_2O_3-based solar-blind ultraviolet photodetectors[J]. Chinese Journal of Lasers, 2021, 48(11): 1100001.
[33] 姚杰, 缪鑫, 王帅, 等. 高响应度光电检测器件石墨烯-MoS_2垂直异质结的制备[J]. 激光与光电子学进展, 2021, 58(15): 1516024.
Yao J, Miao X, Wang S, et al. Preparation of graphene-MoS_2 vertical heterojunction for high-responsivity photodetectors[J]. Laser & Optoelectronics Progress, 2021, 58(15): 1516024.
[34] 林亚楠, 吴亚东, 程海洋, 等. $PdSe_2$纳米线薄膜/Si异质结近红外集成光电探测器[J]. 光学学报, 2021, 41(21): 2125001.
Lin Y N, Wu Y D, Cheng H Y, et al. Near-infrared integrated photodetector based on $PdSe_2$ nanowires film/Si heterojunction [J]. Acta Optica Sinica, 2021, 41(21): 2125001.

Construction of V_2O_5/SnO_2 Nanofiber Heterojunctions and Their Optoelectronic Properties

Jin Yanxin, Wu Qiuqi, Tang Chaoyang, Cao Wenjun, Guo Xuda, Hou Jiwei*

School of Physical and Mathematical Science, Nanjing Tech University, Nanjing 211816, *Jiangsu, China*

Abstract

Objective With the rapid development of society, the demands for portable, lightweight, and large-area-compatible wearable electronic devices continue to grow, which drives photodetectors developing towards low-cost, high-performance, low-power, and large-scale manufacturing. One-dimensional inorganic nanomaterials facilitate the separation of electrons and holes due to their large specific surface area, high aspect ratio, abundant surface trap states, and unique electron confinement effects, thus extending the lifetime of photogenerated charge carriers. Additionally, the linear geometric structure provides sound elasticity to external stresses, making them less prone to cracking after deformation. These characteristics make one-dimensional inorganic nanomaterials an ideal choice for designing and preparing high-performance optoelectronic detection devices. In one-dimensional nanomaterial systems, nanofibers/wires have caught much attention from researchers in flexible display devices, gas sensors, and photodetectors due to their unique electrical and optical properties.

As a transition metal oxide, V_2O_5 has a moderate direct bandgap (2.2-2.8 eV), significant optical absorption characteristics in the visible light region, and excellent physical and chemical properties. It is considered a candidate material for excellent optoelectronic devices. Meanwhile, SnO_2 is a common n-type semiconductor material with high electron mobility (240 $cm^2 \cdot V^{-1} \cdot s^{-1}$), which makes it a good electron transfer material with a low hole electron recombination rate and the ability to generate stable photocurrent. The nanofiber system exhibits sound crystallization, and the construction of specific functional heterojunctions can significantly enhance its performance, leading to its applicability in preparing high-performance optoelectronic detection devices. Therefore, photodetectors based on V_2O_5/SnO_2 nanofiber heterostructures should theoretically have a faster light response speed than single component materials. To further investigate the optoelectronic properties of V_2O_5/SnO_2 nanofiber heterostructures, we employ coaxial electrospinning technology to prepare V_2O_5/SnO_2 nanofiber heterostructures with good crystallinity by adopting different vanadium and tin

sources as precursors. Heat annealing treatment is carried out in different atmospheres to construct V_2O_5/SnO_2 nanofiber heterojunctions with various morphology and sizes. By utilizing V_2O_5/SnO_2 nanofiber heterostructures with varying morphology and sizes as a foundation, a high-speed optoelectronic detection device is constructed to assess its responsiveness to visible light in various laser irradiation conditions. We also elucidate the specific physical mechanism behind the rapid response to further expand the potential applications of V_2O_5/SnO_2 nanofiber heterostructures.

Methods 0.7993 g (0.003 mol) of acetylacetone vanadium oxide ($C_{10}H_{14}O_5V$) is weighed and placed in a small beaker. Then a pipette is leveraged to measure 10 mL N, N-dimethylformamide (DMF), and the solution is dropped into a small beaker. Next, the beaker is sealed with aluminum foil and is placed in a heating magnetic stirrer of collector type constant temperature, with the temperature controlled at 75 ℃. Meanwhile, heating is conducted for 10 min to ensure complete dissolution. Subsequently, 1.1500 g polyacrylonitrile (10% PAN) is added to the dissolved $C_{10}H_{14}O_5V$ solution, placed in a heating magnetic stirrer of collector type constant temperature, and heated and stirred at 75 ℃ for 2.5 h to obtain a PAN+$C_{10}H_{14}O_5V$ shell solution with a certain viscosity. Later, 1.0607 g (0.003 mol) pentahydrate tin tetrachloride ($SnCl_4·5H_2O$) is weighed and placed in a small beaker. A pipette is adopted to measure 10 mL DMF, the solution is dropped into a small beaker, and then the beaker is sealed with aluminum foil and placed in a heating magnetic stirrer of collector type constant temperature. The temperature is controlled at 55 ℃ and heating is carried out for 10 min to ensure complete dissolution. 1.1730 g polyacrylonitrile (10% PAN) is added to the dissolved $SnCl_4·5H_2O$ solution, placed in a heating magnetic stirrer of collector type constant temperature, and heated at 75 ℃ for 2.5 h to obtain a uniform PAN+$SnCl_4·5H_2O$ core solution. This experiment employs the MSK-NFES-1U electrospinning machine of Hefei Kejing Materials Technology Co., Ltd., with a 22G+17G coaxial stainless steel electrospinning needle, to spin (PAN+$C_{10}H_{14}O_5V$)/(PAN+$SnCl_4·5H_2O$) coaxial nanofibers. Additionally, the two prepared solutions are injected into two syringes, with the shell solution connected to the outer tube of the coaxial needle and the core solution injected into the inner tube of the coaxial needle. The flow rates of the inner spinning solution and the outer spinning solution are adjusted to 0.5 mL/h and 0.8 mL/h respectively. By adopting the conditions including a voltage of 15.06 kV, a collection speed of 200.00 r/min, a moving speed of 5 mm/s, and a receiving distance of 20 cm, we successfully spin coaxial nanofibers composed of (PAN+acetophenoxy vanadium)/(PAN+stannic chloride pentahydrate). The spun original composite fibers are placed in an electric blast drying oven and dried at 90 ℃ for 8 h. Then the dried fibers are divided into two parts and placed separately in a high-temperature tubular sintering furnace. One part is annealed in an air atmosphere, and the other is annealed in an argon atmosphere. Both are kept at constant temperature for 1 h at 500 ℃, which leads to two V_2O_5/SnO_2 nanofiber heterojunctions that are thermally annealed in different atmospheres.

Results and Discussions At room temperature, the photocurrent of V_2O_5/SnO_2 nanofiber heterojunction devices is significantly enhanced under the presence of laser irradiation. Under the ultraviolet light irradiation with a wavelength of 405 nm and a power of 48 mW at a voltage of 2.0 V, the heterojunction exhibits 1.28 μA photocurrent, significantly higher than the dark current 0.96 μA at the same bias voltage [Fig. 7(a)]. In the same conditions, the photocurrent and dark current of pure V_2O_5 nanofiber devices are 0.43 μA and 0.41 μA respectively, with a difference of 0.02 μA between the photocurrent and dark current, which indicates there is no significant change between them [Fig. 7(b)]. Figure 8 shows the *I*-*V* curves of two types of photodetectors under different laser irradiation powers, with linear relations between photocurrent and bias voltage under different laser irradiation powers. As the power density of laser irradiation increases, the device photocurrent rapidly increases. In the same laser irradiation conditions, the photocurrent of V_2O_5/SnO_2 nanofiber heterojunction photodetector is significantly higher than that of V_2O_5 nanofiber photodetector. With the periodic opening and closing of laser irradiation, the device photocurrent exhibits good repeatability corresponding to the periodic light illumination changes. During the observation period, there is almost no photocurrent attenuation, which demonstrates sound stability and photoelectric switching performance (Fig. 9). Under laser irradiation with a bias voltage of 3.0 V, a wavelength of 405 nm, and a power density of 123 mW, the optical switching ratio of the V_2O_5/SnO_2 nanofiber heterojunction photodetector is 1.9, the responsivity is 3.97 A/W, and the specific detectivity is 2.2×10^7 Jones [Fig. 9(a)]. Under laser irradiation with a bias voltage of 3.0 V, wavelength of 405 nm, and laser power of 123 mW, the response time and decay time of the V_2O_5/SnO_2 nanofiber heterojunction photodetector are 0.556 s, while those of the V_2O_5 nanofiber photodetector are 1.39 s and 2.78 s respectively (Fig. 10). Obviously, after the combination of V_2O_5 and SnO_2, the photocurrent response time and decay time are significantly improved.

Conclusions We successfully prepare a V_2O_5/SnO_2 nanofiber heterostructure using coaxial electrospinning technology. Based on this heterostructure, we design a photodetector and study the photoresponse performance of the V_2O_5/SnO_2 nanofiber heterostructure photodetector in different lighting conditions. The experimental results show that under the modulation of a periodic laser with a bias voltage of 3.0 V, the V_2O_5/SnO_2 nanofiber heterojunction photodetector exhibits fast optical response, with a response and decay time of 0.566 s, a responsivity of 3.97 A/W, and a specific detectivity of

2.2×10^{7} Jones. Meanwhile, the photodetector exhibits sound photoelectric detection performance at room temperature. The excellent performance is attributed to rapid and effective photo-generated exciton dissociation at the oxide heterojunction interface with type Ⅱ band alignment. Finally, our research can provide new ideas for the applications of oxide heterostructures in optoelectronic devices.

Key words V_2O_5; V_2O_5/SnO_2 nanofiber heterojunction; electrospinning; photodetector